THE JOURNAL OF PHYSICAL CHEMISTRY C

Article

Cite This: J. Phys. Chem. C 2019, 123, 7299−7307

pubs.acs.org/JPCC

Atomic-Scale Structure of Mesoporous Silica-Encapsulated Pt and PtSn Nanoparticles Revealed by Dynamic Nuclear Polarization-Enhanced ^{29}Si MAS NMR Spectroscopy

Evan Wenbo Zhao,*[,†,⊥] Raghu Maligal-Ganesh,[‡] Frederic Mentink-Vigier,[§] Tommy Yunpu Zhao,[†] Yong Du,[†] Yuchen Pei,[‡] Wenyu Huang,*[,‡,∥] and Clifford Russell Bowers*[,†]

[†]Department of Chemistry, University of Florida, Gainesville, Florida 32611 United States

[‡]Department of Chemistry, Iowa State University, Ames, Iowa 50011, United States

[§]National High Magnetic Field Laboratory, Tallahassee, Florida 32310, United States

[∥]Ames Laboratory, U.S. Department of Energy, Ames, Iowa 50011, United States

Supporting Information

ABSTRACT: Mesoporous silica-encapsulated Pt (Pt@mSiO$_2$) and PtSn (PtSn@mSiO$_2$) nanoparticles (NPs) are representatives of a novel class of heterogeneous catalysts with uniform particle size, enhanced catalytic properties, and superior thermal stability. In the ship-in-a-bottle synthesis, PtSn@mSiO$_2$ intermetallic NPs are derived from Pt@mSiO$_2$ seeds where the mSiO$_2$ shell is formed by polymerization of tetraethyl orthosilicate around a tetradecyltrimethylammonium bromide template, a surfactant used to template MCM-41. Incorporation of Sn into the Pt@mSiO$_2$ seeds is accommodated by chemical etching of the mSiO$_2$ shell. The effect of this etching on the atomic-scale structure of mSiO$_2$ has not been previously examined, nor has the extent of the structural similarity to MCM-41. Here, the quaternary Q^2, Q^3, and Q^4 sites corresponding to formulas $Si(O_{1/2})_2(OH)_2$, $Si(O_{1/2})_3(OH)_1$, and $Si(O_{1/2})_4$ in MCM-41 and the mesoporous silica of Pt@mSiO$_2$ and PtSn@mSiO$_2$ NPs were identified and quantified by conventional and dynamic nuclear polarization (DNP)-enhanced ^{29}Si magic angle spinning nuclear magnetic resonance. The connectivity of the −Si−O−Si− network was revealed by DNP-enhanced two-dimensional ^{29}Si−^{29}Si correlation spectroscopy.

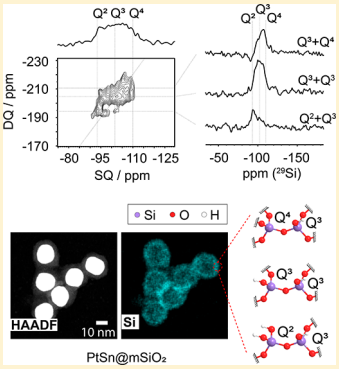

INTRODUCTION

Encapsulation of transition-metal nanoparticles (NPs) in mesoporous silica (mSiO$_2$) has been found to be beneficial for diverse applications ranging from catalysis[1−3] to colorimetric diagnostics,[4] surface-enhanced Raman scattering detection,[5] and photothermal therapy.[6] The mSiO$_2$ shell can impart improved thermal stability and tunable optical properties, as well as facilitate functionalization of encapsulated materials.[7] In the "ship-in-a-bottle" approach to the synthesis of NPs with ordered intermetallic phases, the mSiO$_2$ encapsulation protects the metallic cores from sintering during the high-temperature treatment, yet the shell does not block the access of small organic substrates/products to/from the catalytically active sites.[8]

The intermetallic NPs (iNPs) such as PtSn@mSiO$_2$ exhibit increased selectivity and stability in selective hydrogenation, dehydrogenation, and CO oxidation.[1,9,10] The PtSn@mSiO$_2$ iNP catalyst was found to be highly selective in the hydrogenation of nitro groups in various functionalized nitroarenes.[9] Recently, we demonstrated the efficacy of PtSn@mSiO$_2$ and Pt$_3$Sn@mSiO$_2$ NPs for hyperpolarization by parahydrogen-induced polarization.[11−13] In particular, the PtSn@mSiO$_2$ iNPs delivered record-high pairwise selectivity in the heterogeneous hydrogenation of propene to propane,[14] and the Pt$_3$Sn@mSiO$_2$ iNPs were found to be unique in their ability to mediate the conversion of the nuclear magnetic resonance (NMR)-invisible parahydrogen singlet spin order into hyperpolarized proton magnetization of coadsorbed water, methanol, and ethanol.[13]

The mSiO$_2$ shell around our Pt NPs is formed by the polymerization of tetraethyl orthosilicate (TEOS) at room temperature in the presence of a base, with the cationic surfactant tetradecyltrimethylammonium bromide (TTAB) functioning as the template. The PtSn@mSiO$_2$ iNPs are prepared by heterogeneous nucleation of Sn from its hydrated salt $SnCl_2{\cdot}2H_2O$ at the metal surface of Pt@mSiO$_2$ in tetraethylene glycol at 280 °C. This ship-in-a-bottle synthesis was first employed to prepare bimetallic PtPd from Pt@mSiO$_2$ seeds[11] where it was observed that the silica shells are thinned and eventually completely etched away when an excess Pd precursor (as K_2PdCl_4) was used. The dissolution of silica was further confirmed by inductively coupled plasma mass spectrometry (ICP−MS). However, despite its key role in

Received: February 24, 2019
Published: March 4, 2019

DOI: 10.1021/acs.jpcc.9b01782
J. Phys. Chem. C 2019, 123, 7299−7307

the synthesis, stability, and catalytic properties, little is known about the atomic-scale structure within the $mSiO_2$ shell of Pt@$mSiO_2$ or PtSn@$mSiO_2$, and the possible compositional and structural changes that might occur with the chemical etching accompanying the incorporation of Sn into Pt@$mSiO_2$ seed particles have not been previously investigated. Although the $mSiO_2$ shell is clearly visible in the transmission electron microscopy (TEM) images and the elemental distribution has been mapped out by energy-dispersive X-ray spectroscopy,[15] these techniques do not provide information about the atomic-scale structure, where diffraction techniques (e.g., powder X-ray diffraction crystallography) are inapplicable. Consequently, the bonding topologies of Si within the $mSiO_2$ encapsulation shells and at the $mSiO_2$/metal interfaces in the Pt@$mSiO_2$ and PtSn@$mSiO_2$ NPs had eluded characterization.

NMR spectroscopy can provide atomic-scale structural information on solids which lack long-range order, which makes it well-suited for the characterization of the surfaces of catalysts and NP−adsorbate interactions. However, in comparison to the standard surface science techniques, conventional NMR methods are often inapplicable because of the inherently low sensitivity due to the unfavorable Boltzmann equilibrium polarization of nuclear spins. In dynamic nuclear polarization (DNP), nuclear spin hyperpolarization (i.e., enhanced, nonthermal equilibrium nuclear spin polarization) is induced by continuous microwave saturation of the unpaired electron spin resonance transition and a series of coherent polarization transfers (rotor events) when combined with magic angle spinning (MAS).[16−18] When combined with cross-polarization (CP), MAS DNP NMR typically afford a 1−2 orders of magnitude boost in sensitivity with spatial selectivity to the atoms residing at or near the surface, which provides a powerful contrast enhancement for probing surface structure, surface−adsorbate interactions, and catalytically active sites.[19−32] DNP MAS NMR has been recently applied to functionalized silica and SiO_x/Al_2O_3 materials to obtain chemical bonding information.[19,20,33−40]

Here, we present the results of both conventional and Si-29 DNP MAS NMR experiments on Pt@$mSiO_2$, PtSn@$mSiO_2$, and MCM-41 aimed at comparing the atomic-scale structure of the mesoporous silica in these three materials. Of particular interest are the possible changes in the distribution of Q^x functionalities (where Q signifies a quaternary Si atom bonded to four oxygen atoms and x refers to the number of other Q units connected to the Si tetrahedron) induced upon the incorporation of Sn into the Pt@$mSiO_2$ seed particles. We obtained the distribution of Si functionalities, and the Q^x network connectivity was revealed by the combination of one- and two-dimensional (2D) MAS NMR techniques. Significant differences might exist in the Si-bonding distributions because of the geometrical curvature of the metal NP surfaces and the chemical etching of the inner silica layers accompanying the incorporation of Sn into Pt@$mSiO_2$ seed particles. Two different biradical molecules, AMUPol[41] and TEKPol[42] (see Figure S3), were separately introduced into the samples of the solid powders by incipient wetness impregnation.[19] We compare the structure and composition of the mesoporous silica shells encapsulating Pt and PtSn NPs to that of MCM-41, which is included in this study as a reference material that has been extensively studied by MAS NMR.[43−49] The silica shells in all the three materials was templated from the tetraalkylammonium salts TTAB (Pt@$mSiO_2$ and PtSn@$mSiO_2$) and CTAB (MCM-41), followed by postsynthetic oxidation in air at 500 °C and reduction in H_2/He at 300 °C.

RESULTS AND DISCUSSION

Morphology and Porosity of the NPs. In the TEM images of the Pt@$mSiO_2$ and PtSn@$mSiO_2$ NPs presented in Figure 1A,B, the silica shells have a granulated and disordered

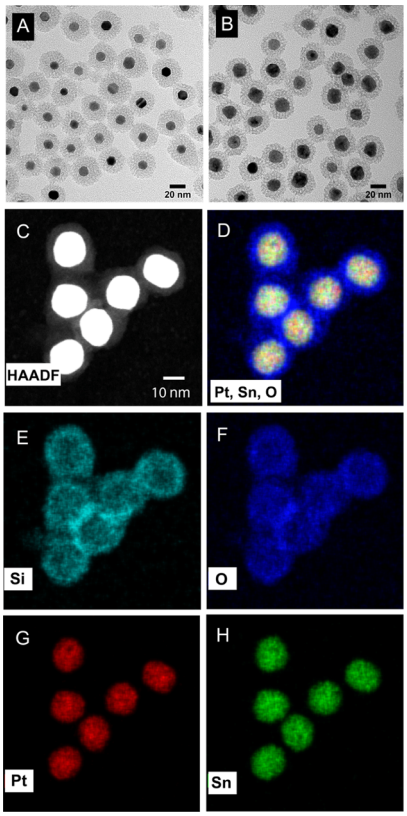

Figure 1. TEM images of (A) Pt@$mSiO_2$ and (B) PtSn@$mSiO_2$ NPs. (C) HAADF-STEM image of the PtSn@$mSiO_2$ iNPs. (D−H) EDS elemental mappings of the PtSn@$mSiO_2$ iNPs.

appearance. The Pt@$mSiO_2$ seed NPs have an average metal core of 14.3 ± 0.8 nm in diameter and a SiO_2 shell of roughly 10.9 ± 0.8 nm in thickness. The PtSn@$mSiO_2$ NPs have a larger average metal core of 20.6 ± 0.9 nm in diameter. The observably thinner SiO_2 shell thickness of 8.3 ± 0.8 nm results from chemical etching during the incorporation of Sn into the metal core. As seen in high-angle annular dark field scanning TEM (HAADF-STEM) and energy-dispersive X-ray spectroscopy (EDS) elemental mapping of PtSn@$mSiO_2$ in Figure 1C−H, the SiO_2 shell encapsulates the PtSn metal core. The well-defined channels in MCM-41[50] are not observed in the TEM images of the $mSiO_2$ shells of our Pt@$mSiO_2$ and PtSn@$mSiO_2$ samples. Although Pt@$mSiO_2$ and PtSn@$mSiO_2$ have significantly lower specific surface area than MCM-41, because of the presence of the nonporous heavy metal NPs in the catalysts, the mesoporous silicas in all the three samples have a similar pore diameter of around 2.4 nm (Figure 2 and Table 1). Neither TEM nor EDS elemental mapping provides information about the atomic-scale bonding in the amorphous silica.[14]

Conventional ^{29}Si MAS NMR. Prior to the NMR experiments, Pt@$mSiO_2$, PtSn@$mSiO_2$ NPs, and MCM-41

DOI: 10.1021/acs.jpcc.9b01782
J. Phys. Chem. C 2019, 123, 7299−7307

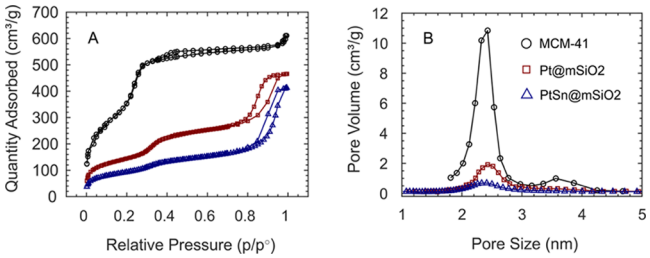

Figure 2. (A) N_2 sorption isotherms at 77 K and (B) Brunauer–Joyner–Halenda pore size distributions of MCM-41, Pt@mSiO$_2$, and PtSn@mSiO$_2$, respectively. The total adsorbed N_2 and pore volume are divided by the total mass of the catalysts.

Table 1. Summary of Physisorption Measurements

sample	BET surface area (m^2/g)	pore volume (cm^3/g)	pore size (nm)
MCM-41	~1160	0.97	2.4
Pt@mSiO$_2$	~506	0.69	2.4
PtSn@mSiO$_2$	~329	0.48	2.4

were oxidized in air at 500 °C and reduced in H_2/Ar (5/45 mL/min) at 300 °C for 4 h, which is a standard pretreatment for the catalysts. The room-temperature one-dimensional (1D) ^{29}Si MAS NMR spectra of two different synthetic batches of Pt@mSiO$_2$, PtSn@mSiO$_2$ NPs, and MCM-41 were recorded prior to impregnation with radicals and are presented in Figures 3 and S1, respectively. The multipeak fitting of the spectral region corresponding to the Q^x sites yields three peaks: Q^2 at −90 ppm; Q^3 at −100 ppm; and Q^4 at −109 ppm.[29,51]

The peak areas in Table 2 are proportional to the number of Q^x sites of each type. The Q^3 and Q^4 sites comprise approximately 98% of all the silicon atoms in both the Pt and PtSn NPs as well as MCM-41, whereas the Q^2 sites are present at a level of only a few percent. The pore size of the mesoporous shells in the Pt@mSiO$_2$ and PtSn@mSiO$_2$ samples, as measured by N_2 physisorption analysis, is 2.4 nm. Despite the significantly different mSiO$_2$ shell thicknesses, our results show that the Pt@mSiO$_2$ and PtSn@mSiO$_2$ NPs have a similar distribution of Q^x sites. Our MCM-41 sample also has a pore size of 2.4 nm. The chemical shifts of the Q^x sites in MCM-41 were found to be close to those of ^{29}Si in the silica shells of Pt and PtSn iNPs, validating the compositional similarity. The measured ratios Q^3/Q^4 in site densities in Pt@mSiO$_2$ and PtSn@mSiO$_2$ are similar, with a greater density of Q^4 over Q^3 sites by almost a factor of 2. In contrast, the MCM-41 sample has a greater density of Q^3 over Q^4 sites (see Table 2). This high Q^3/Q^4 ratio difference could be attributed to the different synthesis conditions, as MCM-41 was synthesized at 80 °C instead of the room temperature used in the growth of mSiO$_2$ for Pt@mSiO$_2$. Additionally, the different Q^3/Q^4 ratios could also be because of the differences in the packing of silica around the curved NP surface. The mSiO$_2$ encapsulation shell surrounding the metal NPs must accommodate curvature, which precludes the formation of a regular hexagonal arrangement of cylindrical pores that characterizes the MCM-41 family of silicas. This likely explains why such channel structures are not observed in the TEM images of our Pt@mSiO$_2$ and PtSn@mSiO$_2$ samples.

To ensure that the relative peak intensities were not significantly distorted because of the differences in T_1 spin

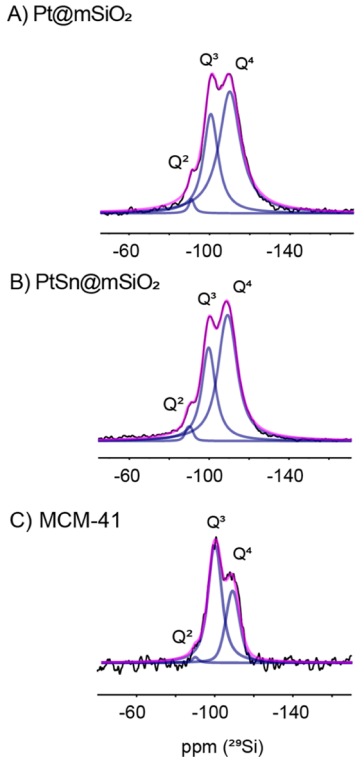

Figure 3. Room-temperature 1D single-pulse ^{29}Si MAS NMR spectra of (A) Pt@mSiO$_2$ (batch #1), (B) PtSn@mSiO$_2$ (batch #1), and (C) MCM-41. These spectra were recorded prior to impregnation of radicals. Black: experimental spectra; magenta: fitted spectra; blue: spectral components resulting from the multipeak fitting.

Table 2. Fraction of the Q^x Sites Calculated from the Integration of the Individual Components of the Multipeak Fitting Decomposition Analysis

NP type	batch number	% Q^2 (−90 ppm)	% Q^3 (−100 ppm)	% Q^4 (−109 ppm)
Pt@mSiO$_2$	1	1.5 ± 0.24	36.2 ± 2.2	62.3 ± 2.5
Pt@mSiO$_2$	2	1.9 ± 0.7	25.4 ± 2.2	72.7 ± 3.7
PtSn@mSiO$_2$	1	1.7 ± 0.5	37.0 ± 2.4	61.3 ± 4.1
PtSn@mSiO$_2$	2	1.8 ± 0.9	37.5 ± 1.7	60.7 ± 1.6
MCM-41	1	1.6 ± 0.1	61.7 ± 2.8	36.6 ± 3.8

relaxation, the spectra of PtSn@mSiO$_2$ NPs were also recorded using the recycle delays of 45 and 15 s (Figure S2). The Q^x distributions obtained for the two different recycle delays were not significantly different. The presence of oxygen in the samples, which were packed into the MAS rotors in ambient air, is known to shorten the T_1 relaxation times to a few seconds.[52,53]

DNP ^{29}Si MAS NMR. To examine the chemical origin, spatial distribution, and connectivity of the Q^x sites, ^{29}Si MAS-DNP NMR experiments were performed. The samples were impregnated with either AMUPol or TEKPol. The molecular sizes of these biradicals are estimated from simple molecular mechanics energy optimization to be 1.7−2.3 and 2.1−2.4 nm, respectively, depending on the conformation (Figure S3). As the molecular sizes are comparable to the ~2.4 nm openings of the mesopores (Figure 2 and Table 1), the extent of the infiltration of the biradicals into the mSiO$_2$ shell is difficult to predict based solely on the theoretical estimates of the

DOI: 10.1021/acs.jpcc.9b01782
J. Phys. Chem. C 2019, 123, 7299−7307

molecular dimensions. The H_2O and trichloroethylene (TCE) solvent molecules are certainly small enough to diffuse into the mesopores.[54] Thus, even if AMUPol or TEKPol molecules would be excluded from the mesopores because of steric interactions, the polarization enhancement of the ^{29}Si nuclei within the $mSiO_2$ shell can still be mediated by a combination of relayed spin diffusion and $^{1}H-^{29}Si$ CP.[55] Figure 4 presents

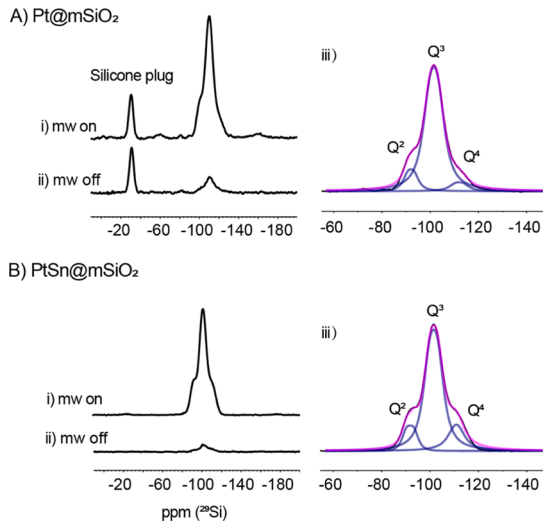

Figure 4. ^{29}Si DNP CP-MAS spectra of $Pt@mSiO_2$ and $PtSn@mSiO_2$ at 100 K with (i) microwaves on or (ii) microwaves off. (iii) Multipeak fitting analysis. Black: experimental spectra; magenta: fitted spectra; blue: spectral components of the multipeak fitting.

the ^{29}Si DNP CP-MAS spectra acquired using AMUPol-impregnated $Pt@mSiO_2$ and $PtSn@mSiO_2$. The signal enhancement factors are $\epsilon_{on/off}$ = 10 and 16, respectively. A signal-to-noise ratio (SNR) of 335, calculated from the peak intensity of the Q^3 sites in $PtSn@mSiO_2$, was obtained after signal averaging for 4 min (16 scans). In contrast, the SNR of only 66 obtained in the conventional Boltzmann-polarized MAS NMR experiment required copious signal averaging for 69 h. TEKPol-impregnated $PtSn@mSiO_2$ yielded a smaller enhancement factor of only 10 (Figure S4). Note that the sensitivity gain afforded by DNP comes at the expense of a slightly degraded spectral resolution arising from paramagnetic broadening.

DNP CP is a two-step process in which the buildup of DNP-enhanced proton polarization is followed by Hartmann–Hahn polarization transfer during a *contact time* (t_c). The CP transfer is mediated by heteronuclear dipolar coupling and depends on the number of proximal hydrogen atoms and their distances.[56,57] Figure 5 compares the ^{29}Si spectra acquired with direct (via e^-—^{29}Si dipolar couplings) and indirect DNP (via CP with hyperpolarized protons), respectively. The direct DNP spectrum shown in Figure 5B was collected using a polarization buildup time of 600 s. The conventional thermally polarized and direct MAS DNP NMR spectra are strikingly similar, whereas the ^{29}Si DNP CP-MAS NMR spectrum (Figure 5C), where only the surface and subsurface sites within the much shorter range of the $^{1}H-^{29}Si$ dipolar contact with solvent molecules are expected to be enhanced, is distinctly different. The different line shapes of the direct and indirect DNP spectra indicate an inhomogeneous spatial distribution of the Q^2, Q^3, and Q^4 sites at the pore surface relative to the bulk. The DNP CP experiment yielded relatively strong Q^2 signals,

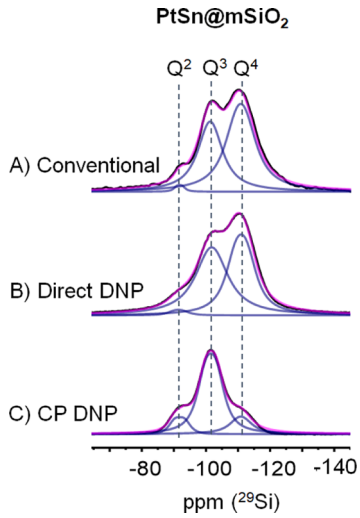

Figure 5. ^{29}Si MAS NMR spectra of $PtSn@mSiO_2$ NPs obtained by (A) single pulse without radicals at room temperature, (B) direct DNP polarization, and (C) indirect DNP CP.

consistent with the Q^2 sites located on the pore surface. Although the Q^4 sites gave the most intense signals in the direct DNP experiment, these sites yielded relatively weak signals in the indirect DNP experiment, consistent with the high fraction of the Q^4 sites which are located away from the pore surface. This further confirms that the Q^4 sites populate the subsurface regions. Because of the relatively large fraction of Q^3 sites at the pore surface, these sites produced strong signals in both the direct and indirect CP experiments. The spatial distribution of the Q^x sites agrees with the established structural model of mesoporous silica.[44,58]

$^{29}Si-^{29}Si$ Correlations via CP-MAS DNP NMR. The gain in ^{29}Si NMR sensitivity afforded by DNP CP allowed us to probe the connectivity among the Q^x sites in the $PtSn@mSiO_2$ catalyst using the 2D $SR26_4^{11}$ $^{29}Si-^{29}Si$ homonuclear correlation experiment. This would have been impractical by conventional MAS NMR with the natural abundance of ^{29}Si (4.9%) for our samples. The dipolar coupling strength between two ^{29}Si nuclei bonded through an oxygen atom is ≈−160 Hz (internuclear distance of ∼3 Å), which yields an ∼1% polarization transfer efficiency when a recoupling time of 2.6 ms is employed in the pulse sequence.[59,60] The internuclear distance between the nearest unbonded ^{29}Si nuclei is ∼5 Å, and thus the coherence transfer between the unbonded Si sites can be safely neglected. The transfer efficiency is further reduced by transverse spin relaxation. The T_2' dephasing time in the $PtSn@mSiO_2$ NPs was measured to be 4 ms in the spin-echo experiment, which is significantly shortened by the impregnated radicals. Therefore, the 2D correlation experiments selectively probe only the ^{29}Si spin pairs bonded via one oxygen atom. In Figure 6A, the isotropic chemical shift of ^{29}Si is shown on the horizontal axis (single quantum (SQ) coherence) and the sum of the isotropic chemical shifts is shown on the vertical axis [double quantum (DQ) coherence].

The signals in the spectrum reflect only the bonded ^{29}Si spin pairs. The spectral slices at −193 ppm (Q^2 + Q^3), −204 ppm (Q^3 + Q^3), and −211 ppm (Q^3 + Q^4) are shown in Figure 6B. The spectra demonstrate the Q^2-Q^3, Q^3-Q^3, and Q^3-Q^4 bonding linkages (Figure 6C). The connectivity agrees with the spatial distribution of the Q^x sites, where the Q^2 and Q^3

DOI: 10.1021/acs.jpcc.9b01782
J. Phys. Chem. C 2019, 123, 7299−7307

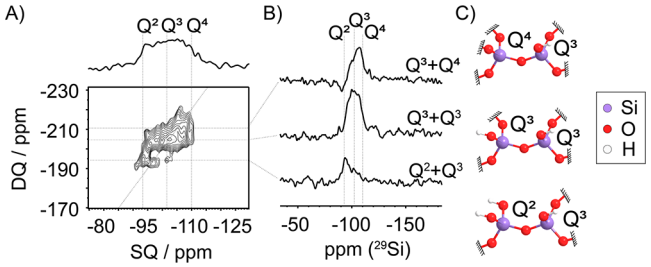

Figure 6. (A) DNP CP-enhanced 2D DQ−SQ correlation spectrum collected using the $SR26_4^{11}$ pulse sequence. The sum of the 1D projection along the SQ dimension is shown at the top panel. (B) 1D projection along the SQ dimension at −193, −204, and −213 ppm in the DQ dimension. (C) Molecular models show the connectivity of the Q sites.

sites are located at or near the pore surface, and Q^4 sites are in the subsurface region.

CONCLUSIONS

By combining conventional solid-state NMR spectroscopy with the direct, indirect, and 2D correlation MAS DNP NMR techniques, the differences in surface selectivity were exploited to characterize the atomic-scale chemical structure in the mesoporous silica of the Pt@mSiO$_2$ and Pt@mSiO$_2$ catalysts as well as MCM-41. Specifically, the Si Q^2, Q^3, and Q^4 tetrahedra were identified in the ^{29}Si spectra of the three materials, and the spatial distributions of the Q^x sites were deduced. With about 40% of the Si sites being Q^2 or Q^3, almost half of the silica atoms reside on the surface, implying that an extended network of Q^4 sites does not exist. The results suggest that the overall structure of the SiO$_2$ shells is very similar to that of typical MCM-41-type materials, except that there is no well-defined periodic pattern of channels. The particular MCM-41 reference sample studied here contained a higher density of Q^3 relative to Q^4 tetrahedra than the mSiO$_2$ shells surrounding the Pt and PtSn NPs which exhibited similar percentages of Q^2, Q^3, and Q^4 Si tetrahedra with the Q^4 sites dominating.

Despite the significant thinning of the mSiO$_2$ shell because of chemical etching during the incorporation of Sn into the Pt@mSiO$_2$ seed particles, we found that the chemical composition and atomic-scale structure of the mSiO$_2$ shell of Pt@mSiO$_2$ and PtSn@mSiO$_2$ are essentially the same. We conclude that the integrity of the atomic-scale structure of mSiO$_2$ is preserved through the synthesis of the intermetallic phase. Hence, the different catalytic activities and selectivities of the Pt@mSiO$_2$ and PtSn@mSiO$_2$ NPs in various reactions cannot be attributed to the structural differences in the mSiO$_2$ shells but must instead be entirely because of the altered chemical composition of the intermetallic phase of the NP metal core.[14,15,61] The differences in the spatial selectivity of the direct and indirect polarization mechanisms were exploited to probe the spatial distribution of the Q^x sites. The direct DNP and conventional MAS spectra are very similar to each other, whereas the indirect (CP-MAS) DNP spectra are different. The extent to which the radicals penetrate the pores in our materials remains an open question. Most likely, the direct DNP spectra report on the distributions of functionalities across the entire shell, which is similar to that of mesoporous silica. The Q^4 sites were determined to be buried in the subsurface layers, whereas the Q^3 and Q^2 sites are present at or near the pore surface. A 2D ^{29}Si−^{29}Si correlation spectrum, enabled by the DNP signal enhancement, revealed the bonding network connectivity among the Q^x sites in the mesoporous silica shell. The protocols we have presented for the elucidation of the bonding structure should generally be applicable to other silica-encapsulated catalysts as well as other nanomaterials with different metals or core−shell compositions.

EXPERIMENTAL SECTION

Synthesis of Monometallic Pt@mSiO$_2$ NPs. The mSiO$_2$-encapsulated Pt NPs (Pt@mSiO$_2$) were prepared according to a literature protocol.[14] Briefly, around 25 mL of 10 mM K_2PtCl_4 was added to 200 mL of a 125 mM aqueous solution of TTAB. The above mixture was stirred for 10 min and then moved to an oil bath maintained at 50 °C for 10 more min. A 25 mL of 300 mM sodium borohydride solution prepared in ice-cold water (Alfa Aesar, 98%) was then added. After the solution was stirred for 20 h at 50 °C, the dark brown solution was centrifuged at 3000 rpm four times for 30 min, with the supernatant being collected while the residue was discarded. Finally, the supernatant was centrifuged at 14 000 rpm for 15 min twice, collected, and redispersed in deionized water to obtain around 200 mL of the solution. About 1 mL of a 1 M sodium hydroxide solution was added to obtain a pH between 11 and 12. During stirring, 3 mL of a 10% TEOS solution in methanol was added dropwise via a syringe. After 24 h, the sample was centrifuged at 14 000 rpm twice, and the coated particles (Pt@mSiO$_2$) were redispersed in 200 mL of methanol. To this, 10 mL of hydrochloric acid (36% assay) was added, and the solution was refluxed at 90 °C for 24 h.

Synthesis of Intermetallic PtSn@mSiO$_2$ NPs. The methanol-dispersed solution of Pt@mSiO$_2$ was centrifuged and redispersed in 75 mL of tetraethylene glycol in a 250 mL two-neck flask. The amount of Pt in the typical synthesis of Pt@mSiO$_2$ particles was 0.15 mmol. PtSn@mSiO$_2$ was made ensuring a Pt/Sn molar ratio of 1:1, using $SnCl_2{\cdot}2H_2O$ (Alfa Aesar, 98%) as the source of Sn, and heating the solution at 280 °C for 2 h to form the alloy. The resulting solution was diluted with an equal volume of acetone and centrifuged at 14 000 rpm to obtain PtSn@mSiO$_2$ NPs. This was then dried and calcined at 500 °C to remove any organic residues from the synthesis. The sample was then reduced in 10% H_2 in a tube furnace at 300 °C for 4 h to obtain intermetallic PtSn@mSiO$_2$. ICP−MS measurements were also carried out on the powdered samples to confirm their stoichiometry as per the synthesis.

Synthesis of MCM-41. Following the literature procedures,[50] 1 g hexadecyltrimethylammonium bromide (CTAB) was mixed with 3.5 mL 2 M NaOH in 480 mL ultrapure water. The mixture was maintained at 80 °C for 1 h under stirring. 5.0 mL Tetraethylorthosilicate was then added dropwise to the solution, and the mixture was maintained at 80 °C for another 2 h under stirring. The as-formed solids were filtered and washed with 200−300 mL water and 200−300 mL methanol and dried under vacuum. 1g dried solid was re-dispersed in the solution of 100 mL methanol with 0.8 mL concentrated HCl and refluxed for 6 h. The refluxed solids were collected by filtration, washed by methanol, and dried in vacuum. The sample was then placed in scintillation vials which were placed in a tube furnace, and pure Ar was passed through the sample at a rate of 50 mL/min for an hour. Following this, the sample was calcined in static air at 500 °C for 4 h and reduced at 300 °C for 4 h in 10% H_2/Ar, which is the same treatments used on

DOI: 10.1021/acs.jpcc.9b01782
J. Phys. Chem. C 2019, 123, 7299−7307

the Pt@mSiO$_2$ and PtSn@mSiO$_2$ samples ahead of NMR measurements.

TEM and EDS. The TEM images were acquired using a TECNAI G2 F20 at an acceleration voltage of 200 kV, as reported in an earlier work.[14] Prior to the TEM measurements, all the samples were first calcined at 500 °C and then reduced at an appropriate temperature in a 50 mL/min 10% H_2 in an argon stream. High-resolution TEM, HAADF-STEM, and elemental mapping analysis were investigated using the same electron microscope equipped with an EDS detector (Oxford INCA EDS) and a Titan Themis 300 probe-corrected transmission electron microscope with a Super-X EDS detector.

Surface Area and Pore Size Measurements. The surface area measurements of Pt@mSiO$_2$, PtSn@mSiO$_2$, and MCM-41 were performed by nitrogen sorption isotherms using a Micromeritics 3Flex surface characterization analyzer at 77 K. Prior to the surface area measurements, all samples were calcined at 500 °C in air and reduced at 300 °C under 50 mL/min 10% H_2/He in a tube furnace.

Conventional MAS NMR Experiments. Prior to all NMR experiments, Pt@mSiO$_2$, PtSn@mSiO$_2$ NPs, and MCM-41 were oxidized in air at 500 °C and reduced in H_2 at 300 °C for 4 h, respectively, which is a standard pretreatment of the catalysts. All the conventional 1D ^{29}Si MAS NMR experiments were performed on a Bruker 600 MHz AVANCE III spectrometer equipped with a 4 mm H/F-X solid probe at room temperature with a MAS spinning rate of 8000 Hz. A 90° pulse with a duration of 4 μs and a recycle delay of 45 s were applied with 3200 scans for Pt@mSiO$_2$ and 5520 scans for PtSn@mSiO$_2$. A 30° pulse with a duration of 2.5 μs and a recycle delay of 30 s were applied with 2904 scans for MCM-41. The ^{29}Si chemical shift was calibrated using 3-(trimethylsilyl)propionic-2,2,3,3-d_4 acid sodium salt as a standard, with the ^{29}Si chemical shift at 1.5 ppm.[62] The decompositions of the 1D conventional NMR spectra were carried out with MestReNova 8.0 software using the automated algorithm after cubic spline baseline correction. Without changing the chemical shift, the peak height, line width, and Lorentzian/Gaussian ratio were varied to optimize the fit for five times. Errors of the peak fittings within 90% confidence interval were included into the reported values.

MAS DNP NMR Experiments. A 30 mg mass of Pt@mSiO$_2$ NPs was impregnated with 30 μL of 10 mM AMUPol solution in a mixture of dimethyl sulfoxide-d_6, H_2O, and D_2O in a weight ratio of 8/1/1 in a 1.5 mL centrifuge tube. The damp solid was packed into a 3.2 mm sapphire rotor and sealed with a silicone plug. A 50 mg mass of PtSn@mSiO$_2$ was impregnated with 50 μL of 10 mM AMUPol solution in a mixture of glycerol-d_8, H_2O, and D_2O in a weight ratio of 6/1/3. Another 50 mg PtSn@mSiO$_2$ sample was impregnated with 60 μL of 16 mM TEKPol in TCE. The two samples were separately packed into 3.2 mm thin-wall zirconia rotors.

All ^{29}Si MAS DNP experiments were performed on a Bruker 600 MHz/395 GHz DNP Avance spectrometer equipped with a 3.2 mm LTMAS probe. For the experiments using AMUPol, 1D ^{29}Si CP-MAS experiment on Pt@mSiO$_2$ was performed with the sample spinning at 6000 Hz, a temperature of 100 K, and continuous irradiation by microwaves using a gyrotron output power of 6.4 W. The 90° ^{1}H excitation pulse length was 5 μs. A ramped pulse was applied on the ^{1}H channel with a contact time of 4.7 ms. SPINAL64 (83 kHz) was applied for proton decoupling. A recycle delay of 9.1 s was used. The 1D ^{29}Si CP-MAS experiments on PtSn@mSiO$_2$ were performed at a spinning speed of 9000 Hz, a 90° ^{1}H excitation pulse length of 3.5 μs, a contact time of 3.6 ms, and a recycle delay of 13 s. For the experiments with TEKPol, the 1D ^{29}Si CP-MAS spectrum of the impregnated PtSn@mSiO$_2$ sample was analyzed using the same parameters as in the experiments with AMUPol except for a shorter recycle delay of 2.6 s. The 1D ^{29}Si direct polarization MAS experiment on PtSn@mSiO$_2$ was performed at a spinning rate of 9000 Hz, a temperature of 100 K, and a continuous microwave irradiation using a gyrotron output power of 6.4 W. A 5 μs 90° pulse tuned at the frequency of ^{29}Si was applied with different recycle delays, as specified in the results. The DNP enhancement factors were calculated by taking the ratio of the peak integrals of the Q sites, with the microwave on and off. The Multipeak spectral fitting of the 1D ^{29}Si MAS DNP NMR spectrum was performed with MestReNova 8.0 software by fixing the chemical shift to the value obtained in the conventional spectrum. The peak height, line width, and Lorentzian/Gaussian ratio were varied to optimize the fit.

The 2D ^{29}Si SR26$_4^{11}$ DQ correlation experiments were performed on PtSn@mSiO$_2$ (impregnated with AMUPol) at 100 K at a MAS speed of 4000 Hz with a continuous microwave irradiation at 6.4 W of gyrotron output power.[59,63] A 3 μs 90° ^{1}H excitation pulse was applied followed by a ramped CP pulse on the ^{1}H channel with a contact time of 3.7 ms. For the SR26$_4^{11}$ sequence, the duration of the 90° ^{29}Si excitation and recoupling pulse was 5 μs and 9.61 ms (nutation frequency is 6.5 times the rotor frequency), respectively. The explicit forms of SR26$_4^{11}$ for recoupling and reconversion, respectively, are

$$[90_{76.2}270_{256.2}90_{283.9}270_{103.9}]^{13}[90_{283.9}270_{103.9}90_{76.2}270_{256.2}]^{13}$$

$$[90_{103.9}270_{283.9}90_{256.2}270_{76.2}]^{13}[90_{256.2}270_{76.2}90_{103.9}270_{283.9}]^{13}$$

and

$$[90_{166.2}270_{346.2}90_{13.9}270_{193.9}]^{13}[90_{13.9}270_{193.9}90_{166.2}270_{346.2}]^{13}$$

$$[90_{193.9}270_{13.9}90_{346.2}270_{166.2}]^{13}[90_{346.2}270_{166.2}90_{193.9}270_{13.9}]^{13}$$

A total of 32 t_1 increments of 225 μs with 1024 scans each were recorded using a recycle delay of 3.64 s. Two sets of spectra acquired under identical conditions were summed to improve the SNR ratio. Pure absorption phase 2D spectra were obtained by the time-proportional phase incrementation method in which all pulses prior to the t_1 evolution are given phase shifts in increments of 45° as t_1 is incremented. A cosine Fourier transform was applied in the indirect dimension. cwLg13 and SPINAL64 (83 kHz) were used for proton decoupling during ^{29}Si dipolar recoupling and data acquisition, respectively.

■ ASSOCIATED CONTENT

Supporting Information

The Supporting Information is available free of charge on the ACS Publications website at DOI: 10.1021/acs.jpcc.9b01782.

Additional conventional and DNP NMR spectra and molecular structures and molecular mechanics energy-minimized van der Waals surface models of AMUPol and TEKPol (PDF)

DOI: 10.1021/acs.jpcc.9b01782
J. Phys. Chem. C 2019, 123, 7299−7307

AUTHOR INFORMATION

Corresponding Authors

*E-mail: zhao0110@chem.ufl.edu (E.W.Z.).
*E-mail: whuang@iastate.edu (W.H.).
*E-mail: bowers@chem.ufl.edu (C.R.B.).

ORCID

Evan Wenbo Zhao: 0000-0003-2233-8603
Raghu Maligal-Ganesh: 0000-0001-8332-4454
Frederic Mentink-Vigier: 0000-0002-3570-9787
Yuchen Pei: 0000-0001-8517-6686
Wenyu Huang: 0000-0003-2327-7259
Clifford Russell Bowers: 0000-0001-6155-5163

Present Address

[⊥]Department of Chemistry, University of Cambridge, Cambridge, CB2 1 EW, United Kingdom.

Notes

The authors declare no competing financial interest.

ACKNOWLEDGMENTS

This work was supported by NSF grants CHE-1507230 (C.R.B.), CHE-1607305 (W.H.), and CHE-1808239 (C.R.B. and W.H.). T.Y.Z. acknowledges support from the Center for Condensed Matter Sciences (CCMS) summer fellowship. F.M.V. thanks Daniel Lee for his suggestions setting up SR26. The National High Magnetic Field Laboratory is supported by the NSF (DMR-1157490) and by the State of Florida. The DNP system is funded in part by NIH S10 OD018519 (magnet and console) and NSF CHE-1229170 (gyrotron).

REFERENCES

(1) Joo, S. H.; Park, J. Y.; Tsung, C.-K.; Yamada, Y.; Yang, P.; Somorjai, G. A. Thermally stable Pt/mesoporous silica core-shell nanocatalysts for high-temperature reactions. *Nat. Mater.* **2009**, *8*, 126−131.

(2) Shang, L.; Bian, T.; Zhang, B.; Zhang, D.; Wu, L.-Z.; Tung, C.-H.; Yin, Y.; Zhang, T. Graphene-Supported Ultrafine Metal Nanoparticles Encapsulated by Mesoporous Silica: Robust Catalysts for Oxidation and Reduction Reactions. *Angew. Chem.* **2014**, *126*, 254−258.

(3) Li, Z.; Mo, L.; Kathiraser, Y.; Kawi, S. Yolk−Satellite−Shell Structured Ni−Yolk@Ni@SiO_2 Nanocomposite: Superb Catalyst toward Methane CO_2 Reforming Reaction. *ACS Catal.* **2014**, *4*, 1526−1536.

(4) Liu, S. H.; Han, M. Y. Synthesis, Functionalization, and Bioconjugation of Monodisperse, Silica-Coated Gold Nanoparticles: Robust Bioprobes. *Adv. Funct. Mater.* **2005**, *15*, 961−967.

(5) Sanles-Sobrido, M.; Exner, W.; Rodríguez-Lorenzo, L.; Rodríguez-González, B.; Correa-Duarte, M. A.; Álvarez-Puebla, R. A.; Liz-Marzán, L. M. Design of SERS-Encoded, Submicron, Hollow Particles Through Confined Growth of Encapsulated Metal Nanoparticles. *J. Am. Chem. Soc.* **2009**, *131*, 2699−2705.

(6) Radloff, C.; Halas, N. J. Enhanced Thermal Stability of Silica-Encapsulated Metal Nanoshells. *Appl. Phys. Lett.* **2001**, *79*, 674−676.

(7) Liu, S.; Han, M. Y. Silica-Coated Metal Nanoparticles. *Chem.—Asian J.* **2010**, *5*, 36−45.

(8) Dong, B.; Pei, Y.; Zhao, F.; Goh, T. W.; Qi, Z.; Xiao, C.; Chen, K.; Huang, W.; Fang, N. In Situ Quantitative Single-Molecule Study of Dynamic Catalytic Processes in Nanoconfinement. *Nat. Catal.* **2018**, *1*, 135−140.

(9) Lu, P.; Campbell, C. T.; Xia, Y. A Sinter-Resistant Catalytic System Fabricated by Maneuvering the Selectivity of SiO_2 Deposition onto the TiO_2 Surface versus the Pt Nanoparticle Surface. *Nano Lett.* **2013**, *13*, 4957−4962.

(10) Krier, J. M.; Michalak, W. D.; Cai, X.; Carl, L.; Komvopoulos, K.; Somorjai, G. A. Sum Frequency Generation Vibrational Spectroscopy of 1,3-Butadiene Hydrogenation on 4 nm Pt@SiO_2, Pd@SiO_2, and Rh@SiO_2 Core−Shell Catalysts. *Nano Lett.* **2015**, *15*, 39−44.

(11) Bowers, C. R.; Weitekamp, D. P. Parahydrogen and synthesis allow dramatically enhanced nuclear alignment. *J. Am. Chem. Soc.* **1987**, *109*, 5541−5542.

(12) Bowers, C. R.; Weitekamp, D. P. Transformation of Symmetrization Order to Nuclear-Spin Magnetization by Chemical Reaction and Nuclear Magnetic Resonance. *Phys. Rev. Lett.* **1986**, *57*, 2645−2648.

(13) Zhao, E. W.; Maligal-Ganesh, R.; Du, Y.; Zhao, T. Y.; Collins, J.; Ma, T.; Zhou, L.; Goh, T.-W.; Huang, W.; Bowers, C. R. Surface-Mediated Hyperpolarization of Liquid Water from Parahydrogen. *Chem* **2018**, *4*, 1387−1403.

(14) Zhao, E. W.; Maligal-Ganesh, R.; Xiao, C.; Goh, T.-W.; Qi, Z.; Pei, Y.; Hagelin-Weaver, H. E.; Huang, W.; Bowers, C. R. Silica-Encapsulated Pt-Sn Intermetallic Nanoparticles: A Robust Catalytic Platform for Parahydrogen-Induced Polarization of Gases and Liquids. *Angew. Chem., Int. Ed.* **2017**, *56*, 3925−3929.

(15) Pei, Y.; Qi, Z.; Goh, T. W.; Wang, L.-L.; Maligal-Ganesh, R. V.; MacMurdo, H. L.; Zhang, S.; Xiao, C.; Li, X.; Tao, F.; Johnson, D. D.; Huang, W. Intermetallic Structures with Atomic Precision for Selective Hydrogenation of Nitroarenes. *J. Catal.* **2017**, *356*, 307−314.

(16) Thurber, K. R.; Tycko, R. J. Theory for cross effect dynamic nuclear polarization under magic-angle spinning in solid state nuclear magnetic resonance: The importance of level crossings. *J. Chem. Phys.* **2012**, *137*, 084508.

(17) Mentink-Vigier, F.; Akbey, U.; Hovav, Y.; Vega, S.; Oschkinat, H.; Feintuch, A. Fast passage dynamic nuclear polarization on rotating solids. *J. Magn. Reson.* **2012**, *224*, 13.

(18) Mentink-Vigier, F.; Akbey, U.; Oschkinat, H.; Vega, S.; Feintuch, A. Theoretical aspects of Magic Angle Spinning - Dynamic Nuclear Polarization. *J. Magn. Reson.* **2015**, *258*, 102.

(19) Lelli, M.; Gajan, D.; Lesage, A.; Caporini, M. A.; Vitzthum, V.; Miéville, P.; Héroguel, F.; Rascón, F.; Roussey, A.; Thieuleux, C.; Boualleg, M.; Veyre, L.; Bodenhausen, G.; Coperet, C.; Emsley, L. Fast Characterization of Functionalized Silica Materials by Silicon-29 Surface-Enhanced NMR Spectroscopy Using Dynamic Nuclear Polarization. *J. Am. Chem. Soc.* **2011**, *133*, 2104−2107.

(20) Lee, D.; Monin, G.; Duong, N. T.; Lopez, I. Z.; Bardet, M.; Mareau, V.; Gonon, L.; De Paëpe, G. Untangling the Condensation Network of Organosiloxanes on Nanoparticles Using 2D $^{29}Si-^{29}Si$ Solid-State NMR Enhanced by Dynamic Nuclear Polarization. *J. Am. Chem. Soc.* **2014**, *136*, 13781−13788.

(21) Johnson, R. L.; Perras, F. A.; Kobayashi, T.; Schwartz, T. J.; Dumesic, J. A.; Shanks, B. H.; Pruski, M. Identifying Low-Coverage Surface Species on Supported Noble Metal Nanoparticle Catalysts by DNP-NMR. *Chem. Commun.* **2016**, *52*, 1859−1862.

(22) Perras, F. A.; Padmos, J. D.; Johnson, R. L.; Wang, L.-L.; Schwartz, T. J.; Kobayashi, T.; Horton, J. H.; Dumesic, J. A.; Shanks, B. H.; Johnson, D. D.; Pruski, M. Characterizing Substrate-Surface Interactions on Alumina-Supported Metal Catalysts by Dynamic Nuclear Polarization-Enhanced Double-Resonance NMR Spectroscopy. *J. Am. Chem. Soc.* **2017**, *139*, 2702−2709.

(23) Ong, T.-C.; Liao, W.-C.; Mougel, V.; Gajan, D.; Lesage, A.; Emsley, L.; Copéret, C. Atomistic Description of Reaction Intermediates for Supported Metathesis Catalysts Enabled by DNP SENS. *Angew. Chem., Int. Ed.* **2016**, *55*, 4743−4747.

(24) Jin, Y.; Kneusels, N.-J. H.; Marbella, L. E.; Castillo-Martínez, E.; Magusin, P. C. M. M.; Weatherup, R. S.; Jónsson, E.; Liu, T.; Paul, S.; Grey, C. P. Understanding Fluoroethylene Carbonate and Vinylene Carbonate Based Electrolytes for Si Anodes in Lithium Ion Batteries with NMR Spectroscopy. *J. Am. Chem. Soc.* **2018**, *140*, 9854−9867.

(25) Rossini, A. J. Materials Characterization by Dynamic Nuclear Polarization-Enhanced Solid-State NMR Spectroscopy. *J. Phys. Chem. Lett.* **2018**, *9*, 5150−5159.

DOI: 10.1021/acs.jpcc.9b01782
J. Phys. Chem. C 2019, 123, 7299−7307

(26) Rossini, A. J.; Zagdoun, A.; Lelli, M.; Lesage, A.; Copéret, C.; Emsley, L. Dynamic Nuclear Polarization Surface Enhanced NMR Spectroscopy. *Acc. Chem. Res.* **2013**, *46*, 1942−1951.
(27) Maly, T.; Debelouchina, G. T.; Bajaj, V. S.; Hu, K.-N.; Joo, C.-G.; Mak−Jurkauskas, M. L.; Sirigiri, J. R.; van der Wel, P. C. A.; Herzfeld, J.; Temkin, R. J.; Griffin, R. G. Dynamic Nuclear Polarization at High Magnetic Fields. *J. Chem. Phys.* **2008**, *128*, 052211.
(28) Kobayashi, T.; Perras, F. A.; Slowing, I. I.; Sadow, A. D.; Pruski, M. Dynamic Nuclear Polarization Solid-State NMR in Heterogeneous Catalysis Research. *ACS Catal.* **2015**, *5*, 7055−7062.
(29) Al Othman, Z.; Apblett, A. W. Synthesis of mesoporous silica grafted with 3-glycidoxypropyltrimethoxy-silane. *Mater. Lett.* **2009**, *63*, 2331−2334.
(30) Lange, S.; Linden, A. H.; Akbey, Ü.; Trent Franks, W.; Loening, N. M.; Rossum, B.-J. v.; Oschkinat, H. The Effect of Biradical Concentration on The Performance of DNP-MAS-NMR. *J. Magn. Reson.* **2012**, *216*, 209−212.
(31) Takahashi, H.; Fernández-de-Alba, C.; Lee, D.; Maurel, V.; Gambarelli, S.; Bardet, M.; Hediger, S.; Barra, A.-L.; De Paëpe, G. Optimization of An Absolute Sensitivity In a Glassy Matrix During DNP-Enhanced Multidimensional Solid-State NMR Experiments. *J. Magn. Reson.* **2014**, *239*, 91−99.
(32) Kobayashi, T.; Lafon, O.; Lilly Thankamony, A. S.; Slowing, I. I.; Kandel, K.; Carnevale, D.; Vitzthum, V.; Vezin, H.; Amoureux, J.-P.; Bodenhausen, G.; Pruski, M. Analysis of Sensitivity Enhancement by Dynamic Nuclear Polarization in Solid-State NMR: A Case Study of Functionalized Mesoporous Materials. *Phys. Chem. Chem. Phys.* **2013**, *15*, 5553−5562.
(33) Mouat, A. R.; George, C.; Kobayashi, T.; Pruski, M.; van Duyne, R. P.; Marks, T. J.; Stair, P. C. Highly Dispersed SiO_x/Al_2O_3 Catalysts Illuminate The Reactivity of Isolated Silanol Sites. *Angew. Chem.* **2015**, *127*, 13544−13549.
(34) Gajan, D.; Schwarzwälder, M.; Conley, M. P.; Grüning, W. R.; Rossini, A. J.; Zagdoun, A.; Lelli, M.; Yulikov, M.; Jeschke, G.; Sauvée, C.; Ouari, O.; Tordo, P.; Veyre, L.; Lesage, A.; Thieuleux, C.; Emsley, L.; Copéret, C. Solid-Phase Polarization Matrixes for Dynamic Nuclear Polarization from Homogeneously Distributed Radicals in Mesostructured Hybrid Silica Materials. *J. Am. Chem. Soc.* **2013**, *135*, 15459−15466.
(35) Berruyer, P.; Lelli, M.; Conley, M. P.; Silverio, D. L.; Widdifield, C. M.; Siddiqi, G.; Gajan, D.; Lesage, A.; Copéret, C.; Emsley, L. Three-Dimensional Structure Determination of Surface Sites. *J. Am. Chem. Soc.* **2017**, *139*, 849−855.
(36) Kobayashi, T.; Perras, F. A.; Goh, T. W.; Metz, T. L.; Huang, W.; Pruski, M. DNP-Enhanced Ultrawideline Solid-State NMR Spectroscopy: Studies of Platinum in Metal-Organic Frameworks. *J. Phys. Chem. Lett.* **2016**, *7*, 2322−2327.
(37) Kumar, A.; Walder, B. J.; Kunhi Mohamed, A.; Hofstetter, A.; Srinivasan, B.; Rossini, A. J.; Scrivener, K.; Emsley, L.; Bowen, P. The Atomic-Level Structure of Cementitious Calcium Silicate Hydrate. *J. Phys. Chem. C* **2017**, *121*, 17188−17196.
(38) Lafon, O.; Rosay, M.; Aussenac, F.; Lu, X.; Trébosc, J.; Cristini, O.; Kinowski, C.; Touati, N.; Vezin, H.; Amoureux, J. P. Beyond the Silica Surface by Direct Silicon-29 Dynamic Nuclear Polarization. *Angew. Chem., Int. Ed.* **2011**, *50*, 8367.
(39) Lafon, O.; Thankamony, A. S. L.; Rosay, M.; Aussenac, F.; Lu, X.; Trébosc, J.; Bout-Roumazeilles, V.; Vezin, H.; Amoureux, J. P. Indirect and direct ^{29} Si dynamic nuclear polarization of dispersed nanoparticles. *Chem. Commun.* **2013**, *49*, 2864.
(40) Thankamony, A. S. L.; Lafon, O.; Lu, X.; Aussenac, F.; Rosay, M.; Trébosc, J.; Vezin, H.; Amoureux, J. P. Solvent-Free High-Field Dynamic Nuclear Polarization of Mesoporous Silica Functionalized with TEMPO. *Appl. Magn. Reson.* **2012**, *43*, 237.
(41) Sauvée, C.; Rosay, M.; Casano, G.; Aussenac, F.; Weber, R. T.; Ouari, O.; Tordo, P. Highly Efficient, Water-Soluble Polarizing Agents for Dynamic Nuclear Polarization at High Frequency. *Angew. Chem., Int. Ed.* **2013**, *52*, 10858−10861.
(42) Zagdoun, A.; Casano, G.; Ouari, O.; Schwarzwälder, M.; Rossini, A. J.; Aussenac, F.; Yulikov, M.; Jeschke, G.; Copéret, C.; Lesage, A.; Tordo, P.; Emsley, L. Large Molecular Weight Nitroxide Biradicals Providing Efficient Dynamic Nuclear Polarization at Temperatures up to 200 K. *J. Am. Chem. Soc.* **2013**, *135*, 12790−12797.
(43) Zhao, X. S.; Lu, G. Q.; Whittaker, A. K.; Millar, G. J.; Zhu, H. Y. Comprehensive Study of Surface Chemistry of MCM-41 Using ^{29}Si CP/MAS NMR, FTIR, Pyridine-TPD, and TGA. *J. Phys. Chem. B* **1997**, *101*, 6525−6531.
(44) Trébosc, J.; Wiench, J. W.; Huh, S.; Lin, V. S.-Y.; Pruski, M. Solid-State NMR Study of MCM-41-type Mesoporous Silica Nanoparticles. *J. Am. Chem. Soc.* **2005**, *127*, 3057−3068.
(45) Ghanbari-Siahkali, A.; Philippou, A.; Dwyer, J.; Anderson, M. W. The Acidity and Catalytic Activity of Heteropoly Acid on MCM-41 Investigated by MAS NMR, FTIR And Catalytic Tests. *Appl. Catal., A* **2000**, *192*, 57−69.
(46) Sutra, P.; Fajula, F.; Brunel, D.; Lentz, P.; Daelen, G.; Nagy, J. B. ^{29}Si and ^{13}C MAS-NMR Characterization of Surface Modification of Micelle-Templated Silicas during the Grafting of Organic Moieties and End-Capping. *Colloids Surf., A* **1999**, *158*, 21−27.
(47) Wouters, B. H.; Chen, T.; Dewilde, M.; Grobet, P. J. Reactivity of the Surface Hydroxyl Groups of MCM-41 towards Silylation with Trimethylchlorosilane. *Microporous Mesoporous Mater.* **2001**, *44*−*45*, 453−457.
(48) Laha, S. C.; Kadgaonkar, M. D.; Anuji, A.; Ganapathy, S.; Amoureux, J. P.; Kumar, R. Multinuclear Solid-State MAS/CP-MAS NMR Studies of Promoter (Phosphate)-Enhanced Crystallization of Siliceous MCM-41. *J. Phys. Chem. B* **2003**, *107*, 14171−14175.
(49) Zhao, X. S.; Audsley, F.; Lu, G. Q. Irreversible Change of Pore Structure of MCM-41 upon Hydration at Room Temperature. *J. Phys. Chem. B* **1998**, *102*, 4143−4146.
(50) Singappuli-Arachchige, D.; Manzano, J. S.; Sherman, L. M.; Slowing, I. I. Polarity Control at Interfaces: Quantifying Pseudo-solvent Effects in Nano-confined Systems. *ChemPhysChem* **2016**, *17*, 2982.
(51) Lippmaa, E.; Maegi, M.; Samoson, A.; Engelhardt, G.; Grimmer, A. R. Structural Studies of Silicates by Solid-State High-Resolution Silicon-29 NMR. *J. Am. Chem. Soc.* **1980**, *102*, 4889−4893.
(52) Cookson, D. J.; Smith, B. E. Atmospheric Oxygen as the Dominant Source of ^{29}Si Spin-Lattice Relaxation in Solid Silicalite. *J. Magn. Reson.* **1985**, *63*, 217−218.
(53) Klinowski, J.; Carpenter, T. A.; Thomas, J. M. The Origin of ^{29}Si Spin−Lattice Relaxation in Zeolites: A Means of Rapid Acquisition of N.M.R. Spectra and of Probing Internal Sites in Microporous Catalysts. *J. Chem. Soc., Chem. Commun.* **1986**, *12*, 956−958.
(54) Pump, E.; Viger-Gravel, J.; Abou-Hamad, E.; Samantaray, M. K.; Hamzaoui, B.; Gurinov, A.; Anjum, D. H.; Gajan, D.; Lesage, A.; Bendjeriou-Sedjerari, A.; Emsley, L.; Basset, J.-M. Reactive Surface Organometallic Complexes Observed Using Dynamic Nuclear Polarization Surface Enhanced NMR Spectroscopy. *Chem. Sci.* **2017**, *8*, 284−290.
(55) Rossini, A. J.; Zagdoun, A.; Hegner, F.; Schwarzwälder, M.; Gajan, D.; Copéret, C.; Lesage, A.; Emsley, L. Dynamic Nuclear Polarization NMR Spectroscopy of Microcrystalline Solids. *J. Am. Chem. Soc.* **2012**, *134*, 16899−16908.
(56) Pines, A.; Gibby, M. G.; Waugh, J. S. Proton-enhanced NMR of dilute spins in solids. *J. Chem. Phys.* **1973**, *59*, 569−590.
(57) Maciel, G. E.; Sindorf, D. W. Silicon-29 NMR Study of the Surface of Silica Gel by Cross Polarization and Magic-Angle Spinning. *J. Am. Chem. Soc.* **1980**, *102*, 7606−7607.
(58) Shenderovich, I. G.; Buntkowsky, G.; Schreiber, A.; Gedat, E.; Sharif, S.; Albrecht, J.; Golubev, N. S.; Findenegg, G. H.; Limbach, H.-H. Pyridine-^{15}N A Mobile NMR Sensor for Surface Acidity and Surface Defects of Mesoporous Silica. *J. Phys. Chem. B* **2003**, *107*, 11924−11939.

DOI: 10.1021/acs.jpcc.9b01782
J. Phys. Chem. C 2019, 123, 7299−7307

(59) Brouwer, D. H.; Kristiansen, P. E.; Fyfe, C. A.; Levitt, M. H. Symmetry-Based29Si Dipolar Recoupling Magic Angle Spinning NMR Spectroscopy: A New Method for Investigating Three-Dimensional Structures of Zeolite Frameworks. *J. Am. Chem. Soc.* **2005**, *127*, 542−543.
(60) Corma, A.; Díaz-Cabañas, M. J.; Martínez-Triguero, J.; Rey, F.; Rius, J. A Large-Cavity Zeolite with Wide Pore Windows and Potential as an Oil Refining Catalyst. *Nature* **2002**, *418*, 514−517.
(61) Maligal-Ganesh, R. V.; Xiao, C.; Goh, T. W.; Wang, L.-L.; Gustafson, J.; Pei, Y.; Qi, Z.; Johnson, D. D.; Zhang, S.; Tao, F.; Huang, W. A Ship-in-a-Bottle Strategy To Synthesize Encapsulated Intermetallic Nanoparticle Catalysts: Exemplified for Furfural Hydrogenation. *ACS Catal.* **2016**, *6*, 1754−1763.
(62) Hayashi, S.; Hayamizu, K. Chemical Shift Standards in High-Resolution Solid-State NMR (1) ^{13}C, ^{29}Si, and ^{1}H nuclei. *Bull. Chem. Soc. Jpn.* **1991**, *64*, 685−687.
(63) Kristiansen, P. E.; Carravetta, M.; van Beek, J. D.; Lai, W. C.; Levitt, M. H. Theory and Applications of Supercycled Symmetry-Based Recoupling Sequences in Solid-State Nuclear Magnetic Resonance. *J. Chem. Phys.* **2006**, *124*, 234510.

DOI: 10.1021/acs.jpcc.9b01782
J. Phys. Chem. C 2019, 123, 7299−7307